Numerical tools for optical pulse propagation in multimode fiber

A thesis submitted to the Faculty of Cornell University in partial fulfillment of the requirements for the Senior Honors Thesis in Engineering Physics

Zachary Ziegler
Professor Frank Wise, Advisor
Applied and Engineering Physics
Cornell University
May 2017

Abstract

As the state-of-the art performance from high-power ultrafast fiber lasers begins to meet fundamental limits in single-mode fiber, there has been a resurgence of interest in multimode fiber. While mature algorithms and technologies exist for simulating pulses in single-mode fiber, the same is not true for multimode fiber where most simulations simply extend the algorithms designed for single-mode fiber. The spatial degree of freedom in multimode fiber adds additional complexity, however, that demands a different approach than in the single-mode case. In this thesis, three such algorithms, one in a modal basis, one in a full spatial basis, and one assuming radial symmetry, are presented. GPU parallelized MATLAB implementations of each of the algorithms are discussed. Initial results from the simulation of two multimode oscillator cavities exemplify the utility of the algorithms. In their own right, these results demonstrate a range of novel dynamics found in multimode mode-locked lasers as well as the potential for such lasers to significantly surpass the performance of their single-mode counterparts.

Acknowledgements

I would like to thank my thesis advisor Professor Frank Wise for his guidance and encouragement both in and out of the lab. I would also like to thank Logan Wright and Zhanwei Liu who have taught me so much about fiber optics, science, and life; it has been a pleasure to work with you. Finally, I want to thank the other members of the Wise group, Walter Fu, Zimu Zhu, Yuxing Tang, Andrei Isichenko, and Pavel Sidorenko.

Table of Contents

1 Introduction

Today, ultra-short pulses enable many emerging technologies such as biological imaging, micromachining, and nanofabrication [4], [6]. The most common source of these pulses for many applications is a mode-locked Ti:sapphire laser oscillator, a solid-state laser which, while producing high-power short pulses, suffers from practical issues such as cost, form factor, and sensitivity to alignment that limit its application outside of the lab. Fiber lasers have the potential to solve many of these issues, however to date the performance of fiber lasers has lagged behind that of their solid-state counterparts, largely due to the strong effect of the Kerr nonlinearity in fiber.

The most obvious way to increase the performance of fiber lasers would be to increase the core area in which the light propagates, thus reducing the effect of the nonlinearity. Beyond a certain core size, however, multiple guided modes with different propagation constants appear, destabilizing the process of coherent pulse formation. Because of this, researchers quickly found that constructing fiber lasers with single-mode-fiber (SMF) was instrumental to achieving mode-locking. As fiber lasers now strongly push against the limits of the nonlinearity, due to their significantly increased peak power, recent work has been devoted to better understand pulse propagation in multimode fiber (MMF). In this way researchers hope to overcome the SMF limitation for fiber oscillators, enabling a multiple-order-of-magnitude increase in the pulse power and thus significantly outperforming state-of-the-art solid-state lasers.

To this end, a number of studies, mostly numerical [2], [11] or theoretical [3], [12], have been devoted to better understanding multimode pulse dynamics in multimode optical fibers. Numerical studies of MMF most often simply extend the most common method of simulating pulses in SMF, the split-step Fourier method, to the case of MMF. As will be shown shortly, such an extension, while natural, suffers from exceptionally poor scaling with the number of modes. These early studies, therefore, are limited to a small number of modes propagated over relatively short distances. A more thorough and conscious effect to optimize propagation algorithms for multimode fiber is needed to fully explore the rich array of dynamics possible in multimode fibers.

The goal of this thesis is to provide the tools needed to learn about pulse propagation physics in multimode optical fiber and simulate realistic multimode laser cavities. In contrast with pulse propagation simulations in SMF, a number of practical and fundamental issues make the simulation of pulses in multimode fiber significantly more challenging. In the first part of this thesis, three new algorithms will be described that address the fundamental challenges of simulating multimode pulse propagation. Next, the optimization and parallelization of these techniques on a graphics processing unit (GPU) will be described, addressing the practical challenges of multimode simulations. Finally, initial results demonstrating the ability of the algorithms to simulate novel multimode fiber oscillators in a realistic way will be presented and future work will be discussed.

2 Simulation methods

A number of simulation methods have been developed over the past 20 years to simulate pulse propagation in single-mode fiber, the most popular of which are the split-step Fourier method [1] and the Runge-Kutta in the interaction picture method [16]. The addition of the spatial degree of freedom in multimode fiber, however, presents a significant challenge not present in SMF.

In the context of the transition from SMF to MMF, which begins with a multimode fiber that supports only a few modes (FMF), the natural extension is to use a mode-resolved basis for the spatial degree of freedom. The first algorithm proposed here solves such a mode-decomposed equation, using the MPA algorithm. Realistic multimode fibers can easily have > 200 modes, however, and in these cases the mode-resolved basis becomes incredibly inefficient. In this case a single-field 3D equation, using the full spatial dimensions, can be much more efficient. The second algorithm described below solves the single-field 3D equation, using a split-step method. Due to the large memory and computation time requirements of such an approach, a third algorithm is described which drastically reduces the computational resources required by assuming radial symmetry. After the algorithms are described, the advantages and disadvantages of each will be discussed.

2.1 Generalized Multimode NLSE

The extension of the single-mode GNLSE to multimode fiber is the Generalized Multimode Nonlinear Schrdinger Equation (GMMNLSE), which in a slightly simplified form can be written [5]

$$\begin{aligned}\frac{\partial A_p}{\partial z} = {} & i(\beta_0^{(p)} - \Re[\beta_0^{(0)}])A_p - (\beta_1^{(p)} - \Re[\beta_1^{(0)}])\frac{\partial A_p}{\partial t} + i\sum_{n\geq 2}\frac{\beta_n^{(p)}}{n!}\left(i\frac{\partial}{\partial t}\right)^n A_p \\ & + i\frac{n_2\omega_0}{c}\left(1+\frac{i}{\omega_0}\frac{\partial}{\partial t}\right)\sum_{l,m,n}\left\{(1-f_R)S^K_{plmn}A_lA_mA_n^* + f_RS^R_{plmn}A_l[h*(A_mA_n^*)]\right\}\end{aligned} \tag{1}$$

Where A_p is the field envelope of the pth mode, $\beta_n^{(p)}$ is the nth order dispersion coefficient for the pth mode, n_2 is the nonlinear index coefficient, ω_0 is the center angular frequency, f_R is the fractional Raman contribution to the nonlinearity, S^K_{plmn} and S^R_{plmn} are the modal overlap factors for the Kerr term and the Raman term, respectively, h is the Raman response function, t is time in a reference frame moving with the fundamental mode at the central frequency, and z is the distance along the fiber.

This equation makes the usual slowly varying envelope approximation and implicitly makes the paraxial approximation. It considers arbitrarily large orders of dispersion, but does not take into account higher order linear space-time coupling.

The computational challenge associated with solving this equation comes from the its poor scaling. For each mode p, propagating one step requires calculating three nested sums, each over all modes. The overall computational complexity associated with this is therefore $O(P^4)$ for P modes, so the computational complexity grows extremely quickly for more than a few modes.

2.1.1 Massively Parallel Algorithm

The approach used in this thesis to solve the GMMNLSE is the new Massively Parallel Algorithm (MPA), first described by Pavel Lushnikov [8], which is still subject to the poor scaling but uses a parallel method to speed up the calculations. In general propagating a pulse along z requires solving this equation in serial, as the evolution of the fields at any given point depends on the fields directly before that point through the nonlinearity. In order to leverage the increasingly parallel capabilities of modern computers, however, the Massively Parallel Algorithm computes several steps in parallel and then iterates until the error is below a given tolerance. As long as the number of iterations is smaller than the extent of parallelization, which can always be the case, this algorithm can be faster than a more traditional serial split-step algorithm.

Grouping the dispersion term into the linear operator $D(t) = i(\beta_0^{(p)} - \Re[\beta_0^{(0)}]) - (\beta_1^{(p)} - \Re[\beta_1^{(0)}])\frac{\partial}{\partial t} + i\sum_{n\geq 2}\frac{\beta_n^{(p)}}{n!}\left(i\frac{\partial}{\partial t}\right)^n$ and using the notation $F[D(t)A_p(t,z)] = D_\omega A_p(\omega,z)$, where F represents the Fourier Transform, MPA defines the change-of-variables

$$A_p(\omega,z) = \psi_p(\omega,z)\exp[D_\omega(z-z_0)] \tag{2}$$

This amounts to defining $\psi(\omega,z)$ as the result of purely nonlinear propagation, as the linear propagation is taken into account exactly. Applying the change of variables, transforming to the Fourier domain, and integrating converts Equation 1 into

$$\psi_p(\omega,z) = \psi_p(\omega,z_0) + i\frac{n_2\omega_0}{c}\left(1+\frac{\omega}{\omega_0}\right)\int_{z_0}^{z}\sum_{l,m,n}F\left\{(1-f_R)S^K_{plmn}A_l(t,z')A_m(t,z')A^*_n(t,z') + f_R S^R_{plmn}A_l(t,z')[h*(A_mA^*_n)](t,z')\right\}\mathrm{e}^{-D_\omega(z'-z_0)}dz' \tag{3}$$

It should be noted that this is still an exact form of the GMMNLSE, no discretization has been applied yet. From this form, however, one can see that the solution could be computed efficiently in parallel if the space along z were broken up into a number of discrete steps and at each point z' the integrand was computed in parallel. This is beneficial because by a large margin the most computationally expensive calculation is the $O(P^4)$ sum, which exists in the integrand. Because of the nonlinear nature of the integrand, in general such a parallelization can not be done; however, by inspecting the length scales of the problem we can formulate a solution.

The two important length scales in the problem are the nonlinear length z_{NL} and the intermode beat length z_{IM}. The nonlinear length depends on the intensity, but is often no less than 50-100 μm and frequently is orders of magnitude larger. The beat length depends on the fiber itself, however, and can be as small as a few μm. Given these two lengths, therefore, we can define a length L such that $L \ll z_{NL}$ and a small step size Δz such that $\Delta z \ll z_{IM}$, that are related by $M\Delta z = L$ (i.e. M small steps fit into one large step). The z grid can then be denoted as the set of equally spaced points z_0, z_1, ..., z_M, where $z_M = z_0 + L$.

Over a distance of L, $\psi(\omega,z)$, which represents the result of nonlinear phase accumulation, is almost constant. To a first approximation, therefore, MPA sets $\psi(\omega,z_j) = \psi(\omega,z_0)$ for $j =$

$1...M$, which also establishes $A_p(\omega, z_j)$ through Equation 2. Next each integrand is calculated in parallel, and then summed to get a more accurate approximation of $\psi(\omega, z_j)$. This process is then repeated in an iterative fashion. Each iteration, the algorithm recalculates $\psi(\omega, z_j)$ by computing each integrand in parallel and then summing. $\psi(\omega, z_j)$ is converted to $A_p(\omega, z_j)$ through Equation 2, and then the process repeats, each time giving $A_p(\omega, z_j)$ with a higher and higher accuracy. Once the accuracy reaches a given threshold the process is considered converged and $A_p(\omega, z_M)$ is taken as the final value at the right end. This finishes one step from z_0 to $z_0 + L$, after which the next large step L can be taken using $A_p(\omega, z_M)$ as the new $A_p(\omega, z_0)$.

In practice, if $L \approx \frac{1}{10} z_{NL}$ or even $L \approx \frac{1}{5} z_{NL}$ this method converges to a high degree of accuracy in $2-3$ iterations at most. Therefore while the small step size needs to be smaller than the intermodal beat length to truly capture all of the physics, the parallelization extent M can easily be 20-40, resulting in a significant net speedup. It should be noted that such a speedup depends heavily on the effectiveness of the implementation of parallelization. If $M = 10$ but computing the integrand for 10 points "in parallel" computes each at 1/10th the speed that it would take to compute a single integrand in serial, this algorithm will not be effective and in fact it will be slower than a split-step method due to the added overhead.

2.1.2 Gain saturation

Another challenging aspect of simulating multi-mode pulse propagation with a mode-resolved basis (i.e. the GMMNLSE) is accounting for spatially dependent gain saturation. For studying passive propagation this is irrelevant, but for in a multimode laser the gain competition between modes will likely be one of the strongest drivers determining which modes are important, and therefore determining the dynamics of the propagation altogether. Including the spatial dependence of gain saturation is therefore crucial for any method of simulating multimode laser cavities. The challenge dealing with this can be seen as follows: One model of gain saturation commonly used in single-mode simulations is, considering the full spatial-temporal field

$$\frac{\partial A(x, y, z, \omega)}{\partial z} = \frac{1}{1 + \int dt |A(x, y, z, \omega|^2 / I_{sat}} \frac{g}{2} f(\omega) A(x, y, z, \omega) \tag{4}$$

where x and y are the transverse coordinates g is the gain coefficient, $f(\omega)$ represents the gain bandwidth, and I_{sat} is the saturation time-integrated intensity (in $\mathrm{J/m^2}$ for example). In general g could also be a function of transverse coordinates; although that case will not be treated here almost exactly the same method can be applied with little extra work.

To adapt this for multimode propagation, we would like to use the mode decomposition and inner product definitions to convert Equation 4 into the form $\partial_z A_p(\omega, z) = ...$ The mode decomposition is defined as

$$A(x, y, z, \omega) = \sum_n F_n(x, y) A_n(\omega, z) \tag{5}$$

where $F_n(x, y)$ is the transverse mode profile of the nth mode. Here the quasi-monochromatic assumption has been made that the mode profile is not a function of frequency. Of course

in reality the modes do change with frequency, but for most pulses in question this will be an adequate assumption. In the transverse space the inner product is defined as

$$< F_n, F_p >= \int F_n(x,y)F_p(x,y)dxdy \tag{6}$$

and the mode profiles satisfy the orthonormality condition

$$\int F_n(x,y)F_p(x,y)dxdy = \delta_{np} \tag{7}$$

Using these definitions, it is not possible to directly convert Equation 4 into a mode-decomposed form by applying the decomposition and then taking the inner product with respect to each mode, because of the form of the gain saturation. One approach that does permit a mode-decomposed solution is to Taylor expand the saturation term, keeping on the first non-constant term. While this is computational feasible, it will be a poor approximation in laser cavities, which necessarily operate at higher intensities than I_{sat}. If the saturation term is multiplied to the LHS, however, applying the decomposition and inner product gives the following set of coupled first order ODEs

$$\frac{\partial A_p}{\partial z} + \sum_{l,m,n} S^R_{plmn} \frac{\partial A_n}{\partial z} B_{lm} = \frac{g}{2} f A_p \tag{8}$$

where S^R_{plmn} is the same overlap tensor as in Equation 1 and $B_{lm} = \int dt A^*_l A_m / I_{sat}$. Defining the matrix elements $T_{ij} = \delta_{ij} + \sum_{l,m} S^R_{ilmj} B_{lm}$ and arranging the A_p's into the vector $\boldsymbol{A}$ allows Equation 8 to be written as the matrix equation

$$T\frac{\partial \boldsymbol{A}}{\partial z} = \frac{g}{2} f \boldsymbol{A} \tag{9}$$

Unlike the form of the GMMNLSE, where each mode can be propagated explicitly, propagating the modes through gain requires an implicit calculation, i.e. solving a system of linear equations for $\frac{\partial \boldsymbol{A}}{\partial z}$. After that, the modes can then be propagated as usual. For example, using a simple Euler's method integration, the propagation through gain becomes

$$\boldsymbol{A}(z + \Delta z) = \boldsymbol{A}(z) + \Delta z \frac{g}{2} f T^{-1} \boldsymbol{A} \tag{10}$$

Two questions about this analysis remain: does the computational complexity of taking the inverse make this prohibitively computational expensive, and how does this work with the other terms of the GMMNLSE? Here T is a $P \times P$ matrix, so the complexity of taking the inverse is $O(P^3)$. The complexity of building the matrix itself, however, requires is $O(P^2)$ for each element, making it $O(P^4)$ in total. This is the same complexity as calculating the large sum in the nonlinear term in the GMMNLSE, so in terms of scaling this approach does not

add any extra complexity. It turns out, however, that building the matrix T requires almost exactly the same operations as the calculation of the sum in the nonlinear term, so in practice treating gain saturation in this way does not add a significant amount of computation time.

The second question is a little more complicated to address. If the other terms of the GMMNLSE are added into this analysis the problem quickly becomes unmanageable. Intuitively, however, this sort of an approach can be applied in a split-step manor, where the GMMNLSE is solved over then step and then the gain saturation is solved assuming no effect from the other terms in the GMMNLSE. This will surely not be perfect, but the gain saturation model itself is already largely unphysical. While not perfect, therefore, this approach to gain saturation allows the important spatial aspect of gain saturation to be accurately taken into account in a way that does not add significantly to the computation time.

Overall, the combination of MPA with the implicit treatment of gain saturation discussed above allows the GMMNLSE with spatial gain saturation to be solved extremely efficiently, as long as the implementation of parallelization is effective. This combination allows for either realistic simulations of multimode laser cavities made with fiber that supports fewer than $\sim$20 modes, or approximate simulations of cavities with many more modes where at most $\sim$20 modes are considered.

2.2 3D single-field GNLSE

While the speed-up with a parallelized MPA algorithm represents a significant advancement for simulating multimode cavities, any such approach the solves the GMMNLSE will suffer from the poor scaling due to the nonlinearity. Furthermore, such a method necessarily makes the quasi-monochromatic assumption, which will be increasing inaccurate for broadband pulses. To get around these issues, another algorithm has been developed to solve the 3D single-field GNLSE that does not rely on a mode decomposition. Written without decomposing into modes, the traditional 3D NLSE is [15]

$$\begin{aligned}\frac{\partial A(x,y,z,\omega)}{\partial z} = \frac{i}{2\beta_{eff}(\omega)}\nabla_T^2 A + \hat{D}_\omega(\omega)A + i\frac{\beta_{eff}(\omega)}{2}\left(\left(\frac{n(x,y,\omega)}{n_{eff}(\omega)}\right)^2 - 1\right)A \\ + F_t\left\{i\frac{n_2\omega_0}{c}\left(1+\frac{i}{\omega_0}\frac{\partial}{\partial t}\right)\{(1-f_R)|A|^2A + f_RA[h*|A|^2]\}\right\}\end{aligned} \tag{11}$$

where $\beta_{eff}(\omega)$ is the effective propagation constant, $\hat{D}_\omega(\omega)$ is the dispersion operator, $n(x,y,\omega)$ is the spatially dependent index of refraction, $n_{eff}(\omega)$ is the effective index of refraction, and F_t represents the Fourier transform in time. There are a few ways to choose n_{eff} and consequently β_{eff} – one could use the refractive index at the center of the core, the index at the cladding, or some average of the two. For simplicity, the convention used in this thesis is to take n_{eff} and β_{eff} as the values of n and β at the center of the core.

This equation makes the usual slowly varying envelope approximation as well as the paraxial approximation. It can be seen, however, that the dispersion and diffraction terms can be written in the Fourier domain in space and time as

$$\frac{i}{2\beta_{eff}(\omega)}\nabla_T^2 A + \hat{D}_\omega(\omega)A \quad \rightarrow \quad \frac{i}{2\beta_{eff}(\omega)}(-k_x^2 - k_y^2) + i(\beta_{eff}(\omega) - \beta_{eff}(\omega_0) - (\omega - \omega_0)\left.\frac{\partial \beta_{eff}}{\partial \omega}\right|_{\omega_0}) \tag{12}$$

where k_x and k_y are the components of the wavevectors in Fourier space. The form of the RHS can be identified as the result of the paraxial approximation, and therefore a more general form for dispersion and diffraction which does not make the paraxial approximation can be written as

$$\hat{D}(k_x, k_y, \omega) = i\left(\sqrt{\beta_{eff}(\omega) - k_x^2 - k_y^2} - \beta_{eff}(\omega_0) - (\omega - \omega_0)\left.\frac{\partial \beta_{eff}}{\partial \omega}\right|_{\omega_0}\right) \tag{13}$$

Replacing dispersion and diffraction in the 3D GNLSE with equation 13, and writing the waveguide term as $\hat{W}(x, y, \omega)$ and nonlinear term as $\hat{N}(x, y, t)$, the 3D GNLSE becomes

$$\frac{\partial A}{\partial z} = \hat{D}(k_x, k_y, \omega)A + \hat{W}(x, y, \omega)A + \hat{N}(x, y, t)A \tag{14}$$

where each of the operators has become a simple elementwise matrix multiplication in the correct basis. Because the paraxial approximation is not required, all of the higher-order linear space-time coupling terms are automatically included. Gain, in the form of Equation 4 can easily be included in the nonlinear term.

This form of the 3D GNLSE suggests a spectral split-step algorithm, and that is exactly what has been implemented for this thesis. Starting in the full space-time Fourier domain, the product $\hat{D}(k_x, k_y, \omega)A(k_x, k_y, \omega)$ is computed, and then the inverse transform is taken to get $A(x, y, \omega)$. Next, the product $\hat{W}(x, y, \omega)A(x, y, \omega)$ is taken in a hybrid real-space and frequency domain and the inverse transform in time is taken to get $A(x, y, t)$. Finally the product $\hat{N}(x, y, t)A(x, y, t)$ is taken followed by the forward transform in space and time to get $A(k_x, k_y, \omega)$.

This split-step algorithm amounts physically to propagating along the step first seeing only dispersion and diffraction, then seeing only the linear waveguide, and then seeing only the nonlinearity. As in any split step algorithm, therefore, this will only be accurate if the step size is small enough that such a decomposition is approximately valid. In the normal single mode NLSE the only length to consider is the nonlinear length, which is usually longer than $\sim$ 50-100 μm. Taking into account diffraction and the waveguide effect, however, introduces another length, the length over which treating the defocusing from diffraction and focusing from the waveguide can be treated independently in series. This will depend on the properties of the waveguide, but as an order of magnitude it can be $2 - 5$ μm.

In light of these different length scale, therefore, the algorithm is slightly modified from what is written above. The dispersion and diffraction and waveguide effect terms are calculated each small step, which includes the forward and inverse Fourier transforms from real space to k-space as well as the much faster elementwise matrix multiplications, but not the

Fourier transform to the time domain or the more time-consuming aspects of the nonlinear step calculation such as the convolution. Then every l small steps, one nonlinear step is calculated, where l is determined by the ratio of nonlinear length to linear length. In practice the small step size needs to be $0.5 - 2$ μm and l can be 10-20, depending on the power. Breaking the symmetry between these operations can be very effective at reducing computation time especially when the Raman and self-steepening terms are enabled, as the more computationally expensive computations need to be calculated much less frequently.

2.3 Radially-symmetric single-field GNLSE

Solving the 3D GNLSE directly is useful for its accuracy, compared to the GMMNLSE, however it requires a significant amount of computational resources to adequately sample all three dimensions (two transverse spatial dimensions and time). This goes beyond a matter of patience, as the memory required quickly exceeds 10-20 GB, the largest amount of memory available for GPUs at the time of this thesis. There is enough memory to conduct simulations, and some systems will be able to be simulated very accurately with it, but if a fine spatial and temporal mesh is needed we may have to wait a few years for GPU memory to catch up.

In the meantime, one useful simplifying assumption that can be made is the assumption of radial symmetry. Many spatial-temporal fiber systems do not show radial symmetry, but there are some important systems which do. Any multimode fiber laser that has a segment of SMF, for example, will likely find radially symmetric states if the alignment between the fibers is correct. Furthermore, at very high powers a "super-mode-locking" state has been predicted which may offer the best performance from a fiber laser. This state is dominated by the fundamental mode and is radially symmetric. Finding mode-locked states in a multimode laser with radial symmetry is therefore both a good starting point to understand multimode laser dynamics and likely a good approximation for some important states.

The approach used in this thesis to efficiently simulate radially symmetric pulse propagation is to solve the 3D GNLSE in cylindrical coordinates assuming no dependence on the azimuthal coordinate. With this assumption, the Radial Coordinate Generalized Nonlinear Schrdinger Equation (RC GNLSE) becomes

$$\begin{aligned}\frac{\partial A(r,z,\omega)}{\partial z} = &\frac{i}{2\beta_{eff}(\omega)}\nabla_r^2 A + \hat{D}_\omega(\omega)A + i\frac{\beta_{eff}(\omega)}{2}\left(\left(\frac{n(r,\omega)}{n_{eff}(\omega)}\right)^2 - 1\right)A \\ &+ F_t\left\{i\frac{n_2\omega_0}{c}\left(1 + \frac{i}{\omega_0}\frac{\partial}{\partial t}\right)\{(1-f_R)|A|^2A + f_R A[h * |A|^2]\}\right\}\end{aligned} \tag{15}$$

The algorithm presented here will be almost identical to that of the 3D GNLSE, except that the correct transform to convert ∇_r^2 to $-k^2$ will be the Hankel transform. The Hankel transform pair used for the following analysis is defined as

$$F_\nu(k) = \int_0^\infty f(r)J_\nu(kr)rdr \tag{16}$$

$$f(r) = \int_0^\infty F_\nu(k)J_\nu(kr)kdk \tag{17}$$

where J_ν is the Bessel function of the first kind of order ν. For some applications ν can be chosen arbitrarily, however for the Hankel transform to correctly convert ∇_r^2 to $-k^2$ ν should be m, the azimuthal Fourier frequency index. As no azimuthal coordinate is considered here, $m = \nu = 0$,

There has been a significant amount of work devoted to calculating these transforms efficiently, for exactly this purpose. Using a direct calculation the Hankel transform has the same complexity of the Discrete Fourier Transform, $O(N^2)$. One would like to use a similar technique as the FFT algorithm to reduce the complexity of the Hankel transform to something like $O(N\log N)$. While this has not been exactly achieved, Siegman showed that the Hankel transform can be converted into a convolution, which can then be efficiently computed using FFTs. Without replicating all the details of that work, this method requires the following exponential spatial grids in real- and Hankel-space:

$$r_n = r_0 \mathrm{e}^{\alpha n} \tag{18}$$

$$k_n = k_0 \mathrm{e}^{\alpha n} \tag{19}$$

where α, r_0, and k_0 can be chosen as needed to trade-off spatial and spectral accuracy near the origin and far from the origin. More details can be found in Siegman's work, but the same method has been used in this thesis for setting these parameters by fixing the number of radial grid points and the parameters K_1 and K_2. Using this quasi-fast Hankel Transform (FHT), the complexity for field sampled at N points is $O(2N\log 2N)$, where the factors of 2 have been included to demonstrate that while the complexity is nominally the same as that of a FHT in practice the computation is a little slower for comparably-sized signals.

One significant source of inaccuracy with this computation of the Hankel transform is the fact that it ignores the field directly at the origin. In 1981, however, Agrawal and Lax showed that the accuracy of the FHT can be significantly improved at effectively no extra computational cost by including the end correction

$$C(k) = \int_0^{r_0} A(r) J_\nu(kr) r dr \tag{20}$$

As mentioned before the radial symmetry selects $\nu = 0$, so assuming that the field is almost constant in the range $0 < r < r_0$ the end correction can be calculated by direct integration as

$$C(k) \approx A(r_0) \int_0^{r_0} J_\nu(kr) r dr = A(r_0) \frac{r_0}{k} J_1(kr_0) \tag{21}$$

The same analysis can be performed for the inverse transform, giving the same result as Equation 21 with k and r flipped everywhere.

As showed by Agrawal and Lax, adding this correction significantly increases the accuracy of the transform. Running the simulation code with and without the correction, I come to the same conclusion. Even though it may only seem like an increase in accuracy of 1% or less, as the Hankel transform is performed each step and there can easily be > 1 million

steps in a realistic simulation including the end correction is instrumental to achieving an acceptable accuracy with this algorithm.

The rest of the algorithm is exactly the same as the 3D GNLSE algorithm, so I will not repeat the details. It suffices to say that the RC GNLSE is decomposed into the same 3 terms

$$\frac{\partial A}{\partial z} = \hat{D}(k,\omega)A + \hat{W}(r,\omega)A + \hat{N}(r,t)A \tag{22}$$

and the operators are applied as elementwise multiplications in the correct basis. The only difference with the 3D code is that instead of using a Fourier transform to get to k-space, the FHT is used. The same asymmetric split-step approach is used, where a small step over the linear terms is computed more frequently than the step propagating over the nonlinearity.

2.4 Discussion

While the three algorithms presented above all attempt to model pulse propagation in multimode fiber, they each have advantages and disadvantages and each has scenarios for which it is the most effective algorithm.

The MM algorithm presented first is fast for a relatively small number of modes, and because there is only one full dimension (time or frequency) the grid can be as fine as needed. It should be noted that "relatively small" depends on the GPU used. With the highest performance consumer GPU available at the time of this thesis, the Nvidia Titan X, the limit above which the simulation time was prohibitively long was around 15-20 modes. For lower-performing GPUs this will likely be around 10-15 modes. Another benefit of the mode-decomposition is that energy is automatically exactly conserved, if there is no gain or loss. On the other hand, the MM algorithm makes the quasi-monochromatic assumption that the modes are the same at all wavelengths, and the additional assumption that the modes are unaffected by the nonlinearity. This is valid to first order, but for very energetic pulses this may begin to break down.

As mentioned before, the limit on the number of modes for the MM code has two effects: complete accuracy to within approximations made by the GMMNLSE will only be realized if simulating a fiber with a relatively small number of modes, and an approximate solution will be found if a number of modes can be selected that are considered "important" to the dynamics. To this second point, in some initial simulations where 15 modes have been selected of the 90 supported at 1030 nm, it is observed that the energy at the end of each round-trip fluctuates larger than expected for a mode-locked pulses, even though the pulse is otherwise the same from round-trip to round-trip. While a subset of modes may be almost entirely responsible for the physics, therefore, it should be expected that small amounts of higher-order-modes contribute to the complete stability of pulses.

The 3D algorithm solves a lot of the accuracy problems of the MM code, and as it does not rely on the mode-decomposition it is relieved of the approximation that the modes do not depend on frequency or intensity, as well as the paraxial approximation by design. On the other hand, the 3D code requires a 3D grid which places significant restrictions on the

fineness of the spatial and temporal grids. The 3D code is also slow compared to the MM code for fewer than ∼20 modes, although it scales much better as the number of modes involved increases, compared to the MM code.

Lastly, the RC algorithm matches the accuracy of the 3D code with the speed of the MM code, with the obvious downside that it only makes sense for radially symmetric fields. The grid sizes can be somewhere in between that of the 3D code and that of the MM code, limited by patience instead of memory as in the 3D case.

The 3D and RC codes also have the added benefit of being slightly more general. While a number of components such as spatial or spectral filters can be converted to a mode-decomposed form, other extra-cavity elements such as a spatial-temporal saturable absorber or the effect of disorder cannot be decomposed as easily. In general this means that the 3D and RC algorithms will give more realistic results for multimode cavities, for which these extra-fiber components play an important role.

3 GPU optimization

Each of the three algorithms described above have been implemented in MATLAB, and optimized for parallelized execution on a GPU. As mentioned earlier, in addition to the fundamental challenges associated with simulating the physics of multimode propagation there is the practical challenge that the addition of spatial degrees of freedom significant increases computation time. Because of this it is much more important than for the easier single mode NLSE case that simulation code be as efficient as possible. This is solved in the code developed for this thesis with GPU parallelization. Compared to other forms of parallelization such as a computing cluster, a GPU has a significantly lower barrier to entry, allowing this code to be used by a much wider audience.

In each of the three algorithms the GPU is used slightly differently. The MM algorithm, which uses MPA as described above, is strongly limited by the calculation of the sum in the nonlinear term which scales like $O(P^4)$. The implementation used here speeds up this part of the computation in two ways, parallelizing along z and in time. The MPA algorithm itself is specifically designed to be executed in parallel along z, as the integrand can be calculated for each of the small steps at the same time. In addition, the code also parallelized in time, meaning that for each small step the calculation of the integrand at different points in time is computed in parallel wherever possible.

In practice, this dual parallelization is implemented with a small kernel of CUDA code, which, given a single index in space (along z and a single index in time) calculates the computationally expensive parts of the integrand. The kernel is run with MATLAB's Parallel Computing Toolkit, which organizes copies of the kernel in blocks and threads. Each thread represents one instance of the kernel, i.e. the calculation of one point in time and space. The threads are organized into a block; in this case all the threads in the block will perform the calculation for a number of points in time, but the same point in space. Then as many blocks as needed are used to perform the calculation for all the points in time and space. As an example, if $N = 2048$ and $M = 20$, the block size (limited by the GPU) might be 1024, meaning each block runs 1024 threads, and therefore there are two blocks for each point in space. In total, then 40 blocks of 1024 threads are needed to perform the calculation over all

points in time and space. The GPU parallelizes the execution of multiple threads in a block, as well as multiple blocks, so this implementation effectively parallelizes in both space and time.

The 3D and RC codes use the GPU in a simpler way. For these algorithms, the main bottleneck is the execution of FFTs instead of a poorly scaling sum. For this, MATLAB's built-in algorithm will always be better than a custom CUDA implementation, so custom CUDA code is not used the way it is for the MM code. The 3D code parallelized entirely within MATLAB, which takes care of the details and simply results in code that runs faster, without having to change anything besides telling MATLAB the code should run on the GPU. It turns out that because the limiting step of the RC algorithm, the FFT, can be extremely fast, a small amount of custom CUDA code is needed to bring the rest of the operations up to speed.

Overall, the GPU has proven to be an extremely powerful and enabling tool for multimode pulse propagation simulations. The results of this thesis rely to a large degree on the speed-up the GPU brings. For the 3D and RC codes MATLAB itself already uses the GPU effectively, but for the MM code the small CUDA kernel is essential for simulating a useful number of modes.

4 Results

Using the simulation algorithms listed above, a number of potentially interesting simulations involving multimode laser oscillators can be conducted. Two examples will be presented here that demonstrate the potential for novel physics in addition to unprecedented performance. Further study aimed at understanding the physics can go into more detail, what follows is an overview of the possibilities of multimode laser oscillators.

4.1 Fully MM cavity

The first laser cavity that will be studied is an extension of an All Normal-Dispersion (ANDi) fiber laser to the multimode regime. For simplicity the cavity will consist of only one continuous segment of gain fiber, plus a spectral filter, spatial filter, ideal spatial-temporal saturable absorber, and output coupling. The parameters have been chosen to reflect available capabilities in experiment. The gain fiber is 0.5 m long, the spectral filter has a Gaussian profile with a FWHM of 4 nm, and the spatial filter has a circular Gaussian profile with a FWHM of 30 μm. The spatial-temporal saturable absorber has a modulation depth of 1 and a saturation intensity of 500 kW/A_{eff}, and the gain has a time-integrated saturation intensity of 1000 nJ/A_{eff}. The center wavelength in the simulations in 1030 nm. The effective area of the fundamental mode, A_{eff}, is used in these values to convert the more familiar units of energy and power to the spatial-temporal units required in any of the three simulation methods listed above. Here A_{eff} is defined as

$$A_{eff} = \frac{\left(\int |F_0(x,y)|^2 dxdy\right)^2}{\int |F_0(x,y)|^4 dxdy} \tag{23}$$

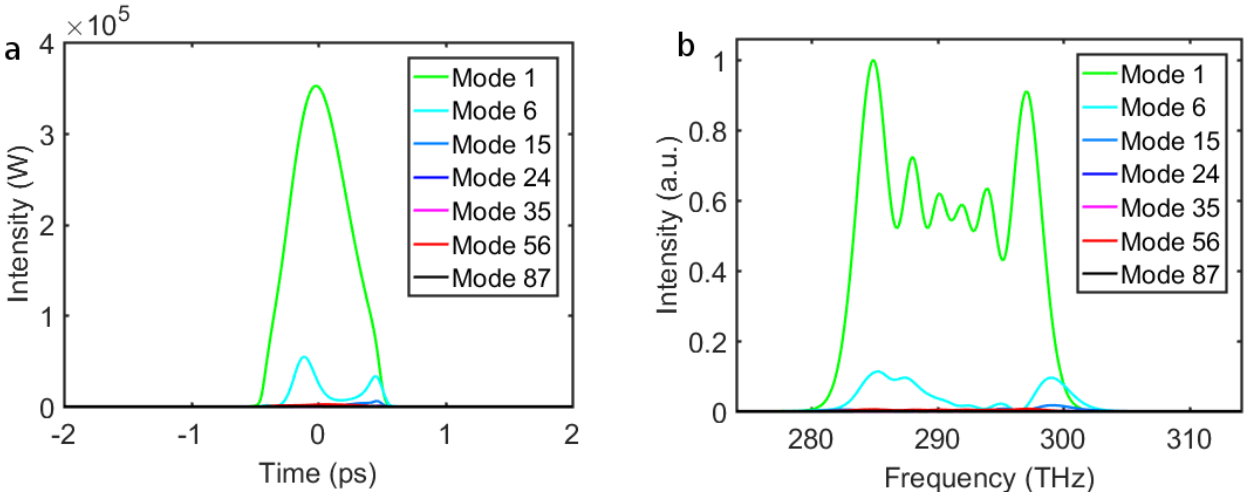

Figure 1: The mode-decomposed field at the output of the multimode cavity, in the (a) time and (b) frequency domains. Each radially symmetric mode has a different color, although only the three lowest-order radially symmetric modes have enough energy to be visible.

where $F_0(x, y)$ is the spatial profile of the fundamental mode.

The gain fiber used is a GRIN-like multimode gain fiber produced by Nufern. In general GRIN or GRIN-like fiber will be preferred because the difference in propagation constants between modes is small, increasing the potential of nonlinear interactions between modes to create coherent multimode pulses. This fiber supports 90 modes at 1030 nm.

The algorithm selected in this case is the RC algorithm, with the goal of finding radially symmetric steady-state mode-locked pulses. As the fiber has 90 modes any MM solution will necessarily be approximate, and as a first pass finding a radially symmetric solution is a good start towards understanding the range of dynamics involved with a multimode laser oscillator. The initial condition is a spacial-temporal Gaussian pulse, with widths comparable to the widths of the filters.

The converged pulse at the output coupling after many iterations is shown in Figure 1, in the time and frequency domains decomposed into the radially symmetric modes. The total energy of the pulse is 219 nJ. The pulse is dominated by the fundamental mode, although there is a non-negligible amount of energy in the second radially symmetric mode and a small amount of energy in the higher-order radially symmetric modes. Through the triangular pulse shape in the time domain and the oscillating features in the frequency domain one can see the traditional signs of pulse propagation through nonlinear fiber at normal dispersion.

On the other hand, the combination of nonlinear coupling between the first two radially symmetric modes and the saturable absorber result in the locking of transverse modes, something that is never a question in single-mode propagation. Compared to single mode laser, any multimode laser will have to contend with the additional de-cohering process of inter-modal walk-off. That a self-consistent mode-locked pulse can be formed, therefore, demonstrates that despite the added challenge multimode mode-locked lasers can produce stable pulses.

To demonstrate the coherent nature of the pulse, the result of temporal dechirping, compensating for quadratic and cubic chirp (i.e. GVD and TOD) is shown in Figure 2

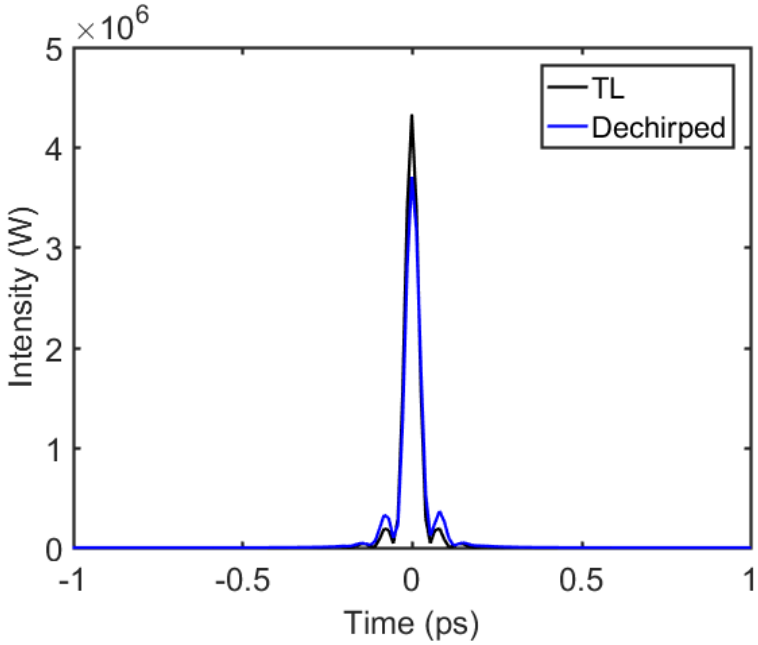

Figure 2: The space-integrated intensity of the space-time transform limited pulse (black) and the result of temporal dechirping (blue) taking into account GVD and TOD. The low time resolution slightly under-samples the pulses, although the close match is still apparent.

compared to the spatial-temporal transform limit. The spatial-temporal transform limit is the limit assuming there is uniform phase in space and time across the pulse. The dechirped pulse, however, is only dechirped in time by apply a uniform quadratic or cubic phase across the pulse. In general we might expect that a full spatial-temporal dechirping would be needed to fully compensate the phase, but it seems here that with only temporal dechirping we are able to achieve a pulse that is very close to the TL. It is unclear at this point if the discrepancy is due to a more complex spatial phase profile or a more complex temporal phase profile.

If such a state or one like it is able to be replicated in experiment, it would represent an order-of-magnitude increase in energy from the highest energy fiber laser oscillators. Furthermore, other early simulations suggest that higher-energy and shorter pulses should be able to be found with similar cavities. While a order-of-magnitude or multi-order-of-magnitude increase in power could be extremely important, it's important to remember that the results presented here are preliminary and only numerical. More work, both experimental and numerical, will be needed to validate these claims.

4.2 SM/MM Mamyshev cavity

A second cavity that has gives interesting results is a Mamyshev cavity with one arm constructed from the usual SMF and the other arm constructed from multimode fiber. A diagram of the cavity is shown in Figure 3.

The concept of a Mamyshev oscillator has existed for many year now [10], however in the past two years a number of results have demonstrated that (with single-mode fiber) such

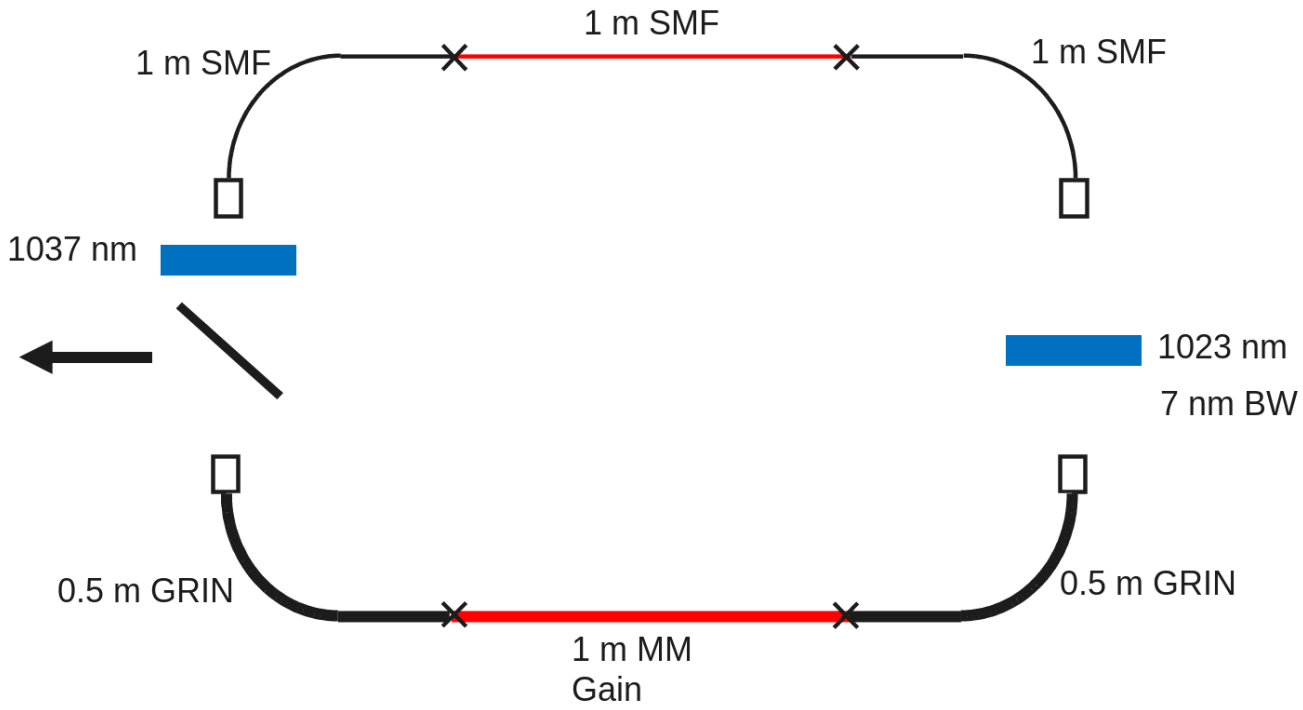

Figure 3: Diagram of the SM/MM Mamyshev cavity.

a design allows for impressive performance without the need for a saturable absorber [9], [13], [14], [7]. Without going into the details, the key behind the Mamyshev operation is the effective saturable absorber created by the combination of spectral broadening and offset spectral filtering. An intense pulse undergoes spectral broadening in the passive and gain fiber of one arm, and is then spectrally filtered at a given center wavelength. Next, the pulse repeats this process in the other arm, except the center wavelength of the filter is shifted with respect to the first filter. With the correct choice of filter separation and bandwidth, the cavity enables a unique pulse propagation in which intense pulses spectrally broaden enough to continue propagating while low-power pulses do not spectrally broaden enough and are attenuated.

The modification here, replacing the fiber in one with multimode fiber, results in a cavity that uses the SMF arm to enable the propagation and the MM arm to generate extremely high energies due to the increased mode-field area and thus reduced effect of the nonlinearity. Both arms could be replaced with multimode fiber, creating a fully multimode cavity, however for a more gentle and controllable transition in knowledge from single-mode to multimode only one multimode arm has been used.

For this simulation, the SMF arm is composed of 1 m of gain fiber between two segments of 1 m passive fiber (all SMF has a 10 μm diameter core. The two spectral filters are centered at 1023 nm and 1037 nm, each with a bandwidth of 7 nm.

The MM arm is composed of 1 m of MM GRIN-like gain fiber between two segments of 0.5 m passive GRIN fiber. The GRIN fiber does not match exactly the profile of the MM gain fiber, but the index profile of the GRIN fiber has been chosen to support a fundamental

mode that very closely matches the fundamental mode of the gain fiber. In this cavity there is no explicit spatial filter (although the coupling between the GRIN fiber and the SMF creates an effective spatial filter), and no explicit saturable absorber.

This time, the MM code has been selected to perform the simulation, largely because of the speed of simulation and ability to have a fine temporal grid spacing. The RC code may be a better choice for this system, however, as the SMF automatically biases towards radially symmetric fields assuming perfect alignment. Furthermore, the three types of fibers require three sets of modes and the projection between bases at the interfaces if using the MM code. Nevertheless, the MM code is used here as a first step for its speed. As the MM fiber supports 90 modes at 1030 nm, 9 low-order modes that had been previously determined as being important from previous simulations plus the remaining 4 radially symmetric modes have been selected to be simulated. This implicitly makes the assumption that there will be a negligible amount of energy in the other modes. While it seems far-fetched, this may not be such a bad approximation due to the radially symmetry imposed by the SMF.

The initial pulse is a highly multimode pulse with 10 nJ equally divided between the modes, starting at the beginning of the passive MM fiber. While this is included for completeness, the initial distribution of energy between the modes is insignificant because the evolution is dominated by the coupling between the output of the SMF and the modes of the passive GRIN fiber.

The steady-state output of the simulation is shown decomposed into the modes of the passive GRIN fiber in the time and frequency domain in Figure 4. The energy of the pulse at the output is 211 nJ. Visualized in this way, the pulse appears to be weakly fundamental-mode dominated, with energy distributed in many modes. Furthermore, the modes are not aligned in time, suggesting that the steady state is largely determined by the propagation of individual modes that are created from the output of the SMF, rather than complicated nonlinear propagation dynamics. The nonlinear interaction of the modes, however, visible in the time domain as oscillations, does play a role.

Another way to visualize the output of the cavity is the output of a (very) fast temporal detector. First, given the mode profiles in time and the mode profiles in space, the full spatial-temporal field can be constructed coherently. Next, the space-averaged intensity is taken by calculating $\int |A(x, y, t)|^2 dxdy$. This gives a sense of the "average" time domain of the pulse. The space-averaged frequency can be computed through a similar procedure using $A(x, y, \nu)$. The result in both domains is shown in Figure 5. Remarkably, despite the complicated oscillating behavior when decomposed into modes, a detector would record a fairly smooth pulse. Despite the walk-off between the modes, therefore, this is truly a multimode laser that is stable despite intermodal interactions.

As a final diagnostic of the pulse quality, the temporally dechirped pulse is compared to the spatial-temporal transform limit in Figure 6. In Figure 6a the pulses are shown in the same form as Figure 5, that is as a space-integrated average. In Figure 6b a little more information is shown, as only one of the spatial dimensions has been integrated over leaving an indication of the full space-time field. In Figure 6a it can be seen that although the pulse appears coherent in Figure 5, when it is dechirped in time only by applying a uniform phase profile distinct peaks appear at different powers as the different modes require a slightly different compensating chirp. In Figure 6b the spatial dependence can be seen, showing that indeed the problem is not that each mode does not dechirp well, but the different modes

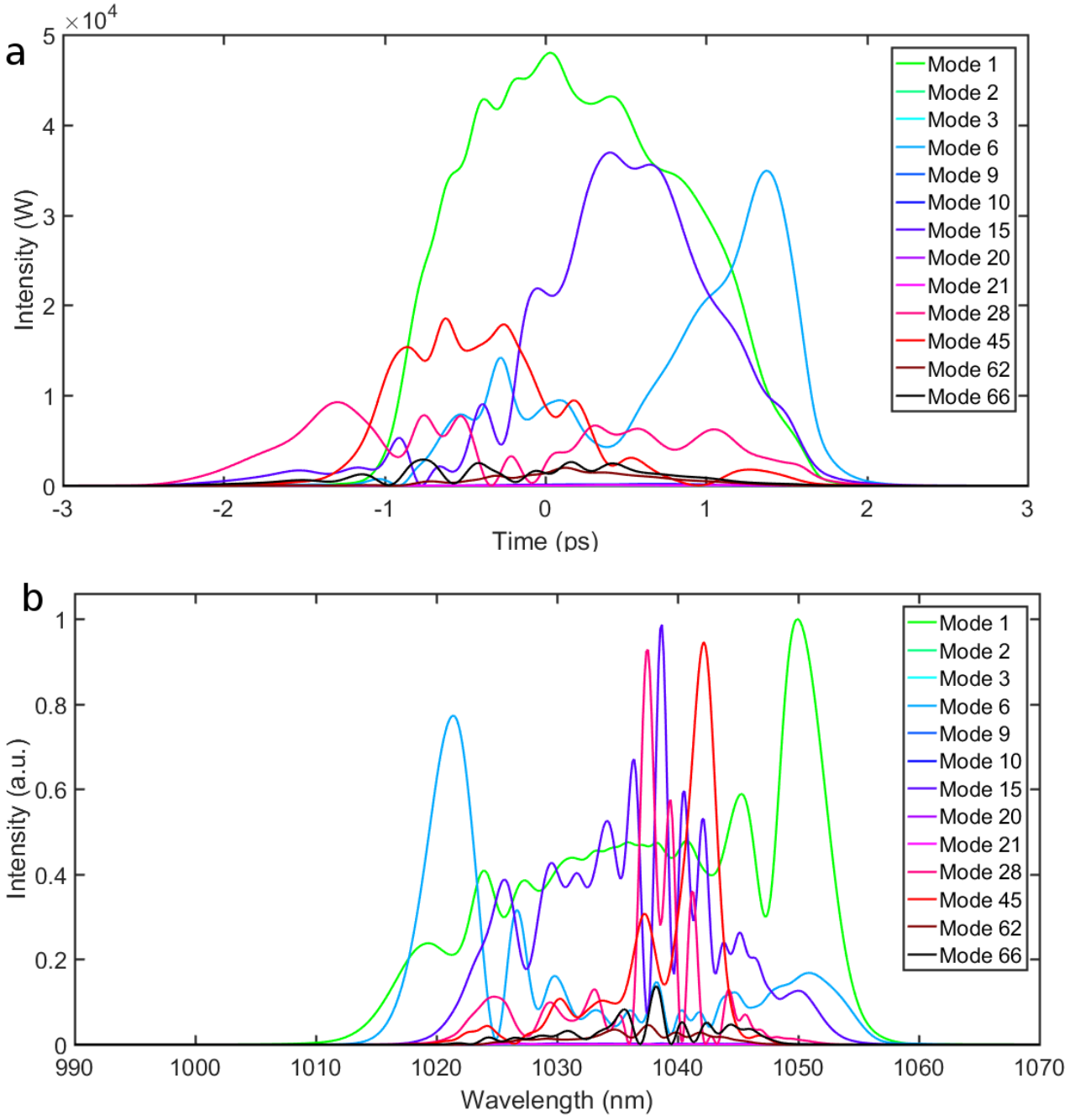

Figure 4: The mode-decomposed field at the output of the SM/MM cavity, in the (a) time and (b) wavelength domains. All of the modes simulated are shown, which form a subset of the 90 total modes supported by the fiber, with different colors.

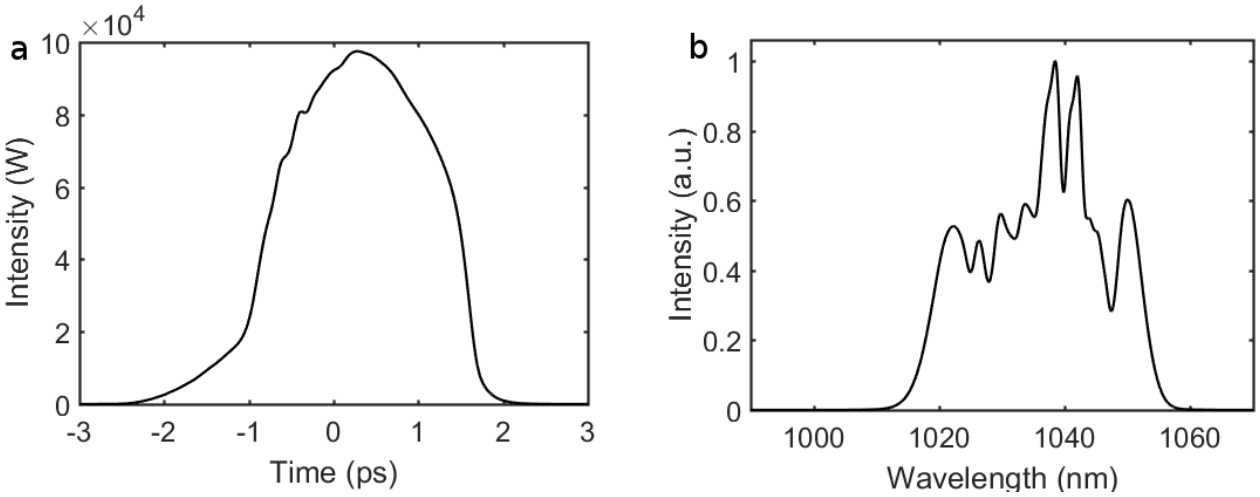

Figure 5: The space-integrated field at the output as a function of (a) time and (b) wavelength. Despite the wild oscillations in the mode-decomposed basis, when coherently added in space and then averaged the resulting pulse appears relatively smooth in both time and wavelength.

with different spatial profiles dechirp to a different extent.

As for the fully MM cavity presented earlier, we should expect that at normal dispersion, the addition of the spatial degree of freedom demands the addition of spatial chirp control at the output. Further work is needed to realize such a spatial-dechirping in experiment, but it may be possible simply with a lens or set of lenses.

Overall these early results demonstrate the potential for high performance and interesting physics when dealing with multimode lasers, as well as the ability of the algorithms presented here to simulate realistic systems. These results aim to inspire the general promise of a multiple-order-of-magnitude improvement in performance and highlight novel interesting physics, with the specific individual results being less important.

5 Future work

The three algorithms presented in this thesis open the door for the efficient simulation of a wide range of interesting systems. In addition to the ANDi-type laser and SM/MM Mamyshev laser demonstrated here, one obvious next step is to investigate the effects of replacing SMF with MMF in other types of fiber cavities such as a Mamyshev cavity where both arms have MM fiber or a MM soliton laser (i.e. at anomalous dispersion). Multimode solitons at anomalous dispersion have previously been reported [15], so while the energy of a MM soliton laser would almost certainly be lower than that of a MM laser at normal dispersion, it is possible that it would have improved stability properties.

More interesting than simply extending from SM to MM, however, would be to investigate how controlling this new spatial degree of freedom could lead to qualitatively new pulse evolutions. For example, with multiple modes the distinction between the near field and the far field becomes more important. So far, all of the cavities that have been simulated

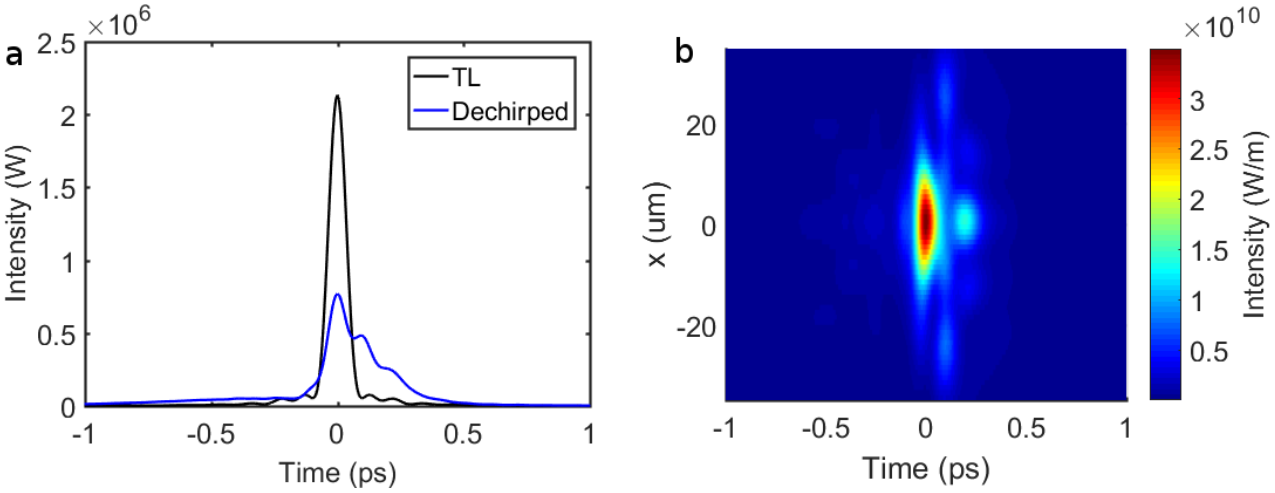

Figure 6: The dechirped output pulse from the SM/MM Mamyshev cavity. The same pulse is shown (a) with both space-dimensions integrated out (blue), compared to the spatial-temporal transform limit (black), and (b) with one space-dimension integrated out as a heat-map.

with MM code have assumed that all spatio-temporal effects occur in the near field. In experiment the spatial filter or saturable absorber can be applied in the near field or the far-field, however, which may lead to different evolutions in simulation.

In addition, the spatial degree of freedom results in the walk-off of linear modes, and therefore the walk-off can be corrected or modified with a lens. In the same way that temporal de-coherence can be avoided in an average cavity sense with an extra-cavity element of opposite dispersion, this form of spatial de-coherence could be mitigated in a similar average cavity sense with a lens or set of lenses in the cavity. Of course this truly makes the system not a fiber laser, but it could lead to interesting pulse propagation nevertheless. It also may be possible to achieve a similar level of control with different specifically defined fibers in the cavity, allowing modes that travel faster in one fiber to travel slower in another.

Finally, while this code has been developed with the goal of simulating multimode laser cavities in mind, it can be applied equally well to other systems. The MM code can be applied to any system with defined modes and a nonlinearity of the same form as the GMMNLSE. Even more generally, the 3D code is well suited for pulse propagation through any medium with any refractive index profile. Furthermore, the simplicity of the 3D code makes the nonlinear term accessible, allowing other nonlinearities to be added in one or two lines of code without altering the efficiency or parallelization.

6 References

[1] Govind Agrawal. *Nonlinear Fiber Optics*. Academic Press, 2007.

[2] Shaival Buch and Govind P Agrawal. Soliton stability and trapping in multimode fibers. *Opt. Lett.*, 40(2):225–228, 2015.

[3] Bruno Crosignani, Antonello Cutolo, and Paolo Di Porto. Coupled-mode theory of nonlinear propagation in multimode and single-mode fibers: envelope solitons and self-confinement. *J. Opt. Soc. Am.*, 72(9):1136–1141, 1982.

[4] W Denk, J H Strickler, and W W Webb. Two-photon laser scanning fluorescence microscopy. *Science*, 248(4951):73–76, 1990.

[5] Peter Horak and Francesco Poletti. Multimode Nonlinear Fibre Optics : Theory and Applications. In Moh Yasin, editor, *Recent Prog. Opt. Fiber Res.* InTech, 2012.

[6] Christopher N. LaFratta, John T. Fourkas, Tommaso Baldacchini, and Richard A. Farrer. Multiphoton fabrication. *Angew. Chemie - Int. Ed.*, 46(33):6238–6258, 2007.

[7] Zhanwei Liu, Zachary Ziegler, Logan G Wright, and Frank W Wise. Megawatt peak power from a Mamyshev oscillator. *pre-print*, 2017.

[8] Pavel Lushnikov. Personal correspondence, 2017.

[9] Thibault North and Camille-sophie Brès. Regenerative similariton laser. *APL Photonics*, 1:021302, 2016.

[10] Stéphane Pitois, Christophe Finot, and Lionel Provost. Asymptotic properties of incoherent waves propagating in an all-optical regenerators line. *Opt. Lett.*, 32(22):3263–3265, 2007.

[11] Francesco Poletti and Peter Horak. Description of ultrashort pulse propagation in multimode optical fibers. *J. Opt. Soc. Am. B*, 25(10):1645–1654, 2008.

[12] S Raghavan and Govind P Agrawal. Spatiotemporal solitons in inhomogeneous nonlinear media. *Opt. Commun.*, 180:377–382, 2000.

[13] Kęstutis Regelskis, Julijanas Želudevičius, Karolis Viskontas, and Gediminas Račiukaitis. Ytterbium-doped fiber ultrashort pulse generator based on self-phase modulation and alternating spectral filtering. *Opt. Lett.*, 40(22):5255–8, 2015.

[14] Igor Samartsev, Andrey Bordenyuk, and Valentin Gapontsev. Environmentally stable seed source for high power ultrafast laser. *Components Packag. Laser Syst. III*, 10085:1–9, 2017.

[15] Logan G Wright, William H Renninger, N Demetrios, and Frank W Wise. Spatiotemporal dynamics of multimode optical solitons. *Opt. Express*, 23(3):145–157, 2015.

[16] Zhongxi Zhang, Liang Chen, and Xiaoyi Bao. A fourth-order Runge-Kutta in the interaction picture method for coupled nonlinear Schrodinger equation. *Opt. Express*, 18(8):8261–8276, 2010.